Spatio-temporal measurement of beam properties in the PLS diagnostic beamline

J. Y. Huang* and I. S. Ko

Pohang Accelerator Laboratory, San 31, Hyoja-dong, Pohang 790-784, Korea. E-mail: huang@postech.ac.kr

A diagnostic beamline is being constructed in the PLS storage ring for measurement of electron- and photon-beam properties. It consists of two 1:1 imaging systems: a visible-light imaging system and a soft X-ray imaging system. In the visible-light imaging system, the transverse beam size and beam position are measured with various detectors: a CCD camera, two photodiode arrays and a photon-beam position monitor. Longitudinal bunch structure is also investigated with a fast photodiode detector and a picosecond streak camera. On the other hand, the soft X-ray imaging system is under construction to measure beam sizes with negligible diffraction-limited error. The X-ray image optics consist of a flat cooled mirror and two spherical focusing mirrors.

Keywords: diagnostic beamlines; beam profiles; beam diagnostics; storage rings; PLS.

1. Introduction

The Pohang Light Source (PLS) is a third-generation synchrotron light source dedicated to many scientific applications since 1994. As a third-generation storage ring requires precise diagnosis and control of machine parameters, the storage ring is equipped with various beam-diagnostic instruments such as the beam position monitor, beam current monitor, photon-beam monitor and beam feedback systems. Among them, photon-beam diagnostics are essential for the study of small-scale electron-beam structure in phase space and its temporal dynamics in ultrashort time scales (Rossa, 1994; Wilke, 1994). A beam-diagnostic beamline composed of a visible-light imaging system and an X-ray imaging system is being constructed for the purpose of photon-beam diagnostics at the PLS.

A visible-beam-diagnostics system has been operating for measurement of the transverse electron-beam profile and the longitudinal bunch structure from the synchrotron radiation source. Transient longitudinal bunch structure is investigated with a synchroscan streak camera with 2 ps resolution. On the other hand, the time-averaged bunch length is measured with a fast optical-to-electrical converter in conjunction with a fast-sampling oscilloscope. Since the visible-light image has a large diffraction-limited error due to the very small radiation angle ($\sim 1/\gamma$) of the low-emittance source, the visible-light beamline will be optimized for only temporal measurements such as bunch length, transient beam structures, fast beam-position measurements, and beam instability studies. An X-ray imaging system is under construction for the precise measurement of the spatial beam structure with minimum diffraction error. Theoretical diffraction-limited errors of the imaging system with 440 nm (2.8 eV) visible light are

around 100 µm vertically, but less than 10 µm with 4.4 nm (284 eV) soft X-rays. In this paper, the status of the beamline and the results of the beam parameter measurements will be described.

2. Imaging optics

The diagnostic beamline extracts the source light from the bending magnet located at the centre of the triple-bend arc sector. Out of the 42 mrad total beam fan from the bending magnet, 14 mrad is used for the diagnostic beamline. Of the 14 mrad, 8 mrad is used for the visible-light imaging system and 2 mrad is used for the X-ray imaging system. Beam sizes at the symmetry point are $\sigma_x = 185$ µm and $\sigma_y = 59$ µm. Various source conditions were considered in the design of optics by ray tracing. Major beam parameters relevant to the design of the diagnostic beamline are summarized in Table 1. A schematic layout of the diagnostic beamline is shown in Fig. 1.

The visible-light imaging optics consists of a water-cooled copper mirror inside the vacuum tank, a remote-controlled beam-steering mirror, and two achromatic lenses outside the vacuum. A 1:1 image is formed by two Melles–Griot achromatic lenses ($f = 3$ m) which are arranged with mirror symmetry. The first focusing lens is located at 7.5 m from the source point and the second mirror is located at 7.5 m from the final image point. The total distance from source plane to the image plane is 25 m. The second lens is remote-controlled for fine adjustment of the location of the final image. The image is then delivered onto the optical table equipped with various detectors inside a dark room.

The X-ray imaging system consists of a flat deflecting mirror and two spherical mirrors forming Kirkpatric–Baez optics (Kirkpatric & Baez, 1948). Vertical and horizontal focusing mirrors are located at 10.581 m and 10.911 m from the source point to make an image at 21.492 m from the source. All three mirrors have a 3° grazing-incidence angle. The acceptance angle of input light is defined as 1.5 mrad in both the horizontal and vertical plane using a water-cooled slit. With the 3° grazing-incidence optics, most of the hard X-rays above 0.8 keV are absorbed at the first deflecting mirror. The maximum heat load at the deflecting mirror is 21.5 W at 400 mA beam current. Less than 10% of the input power is delivered onto the spherical mirrors, where it is dissipated by conduction. Since any kind of surface error of the X-ray mirror results in an imaging error, great care has been taken during the manufacturing of the mirrors. In Table 2, the performance parameters of the mirrors are summarized.

A 5 µm thin carbon foil is used to cut off the low-energy photons below about 200 eV. Since the carbon foil has a strong
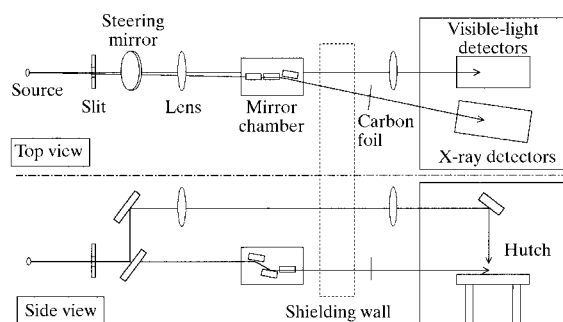
Figure 1
Layout of the diagnostic beamline in the PLS storage ring.

Table 1
Related beam parameters for the diagnostic beamline.

Beam energy	2 GeV
Bending radius	6.306 m
Beam emittance	12.1 nm rad
Source size	
(σ_x, σ_y)	185 µm, 59 µm
$(\sigma_{x'}, \sigma_{y'})$	86.8 µrad, 18.8 µrad
Beam current	1–400 mA
Critical energy	2.8 keV at 2 GeV

Table 2
Design parameters of the mirrors.

	Flat mirror	Spherical mirror
Physical dimensions	310 × 50 × 60 mm	310 × 50 × 60 mm
Radius of curvature	∞	205.2384 m
Effective mirror area	300 × 40 mm	300 × 40 mm
Surface roughness	0.4 nm r.m.s.	0.6 nm r.m.s.
Slope error (5–300 mm)		
Tangential	<1.2 µrad r.m.s.	<1.4 µrad r.m.s.
Sagittal	<1 µrad r.m.s.	<1 µrad r.m.s.
Optical coating	250 nm nickel	250 nm nickel
Blank material	Glidcop	Silicon
Maximum heat load	21.5 W	2.1 W
Cooling	Water-cooled	No cooling

absorption edge at 284 eV and high-energy photons above 0.8 keV are absorbed by the grazing-incidence metal mirrors, it behaves as a band-pass filter with pass band between 200 and 284 eV. Fig. 2 shows the expected spectral intensity of the X-rays at the detector after passing through three kinds of mirror-coating materials and a 5 µm carbon foil. By comparing the transmission of light for three coating materials – carbon, gold and nickel – nickel was chosen as the best one for this application.

Ray tracing of the X-ray imaging optics was performed with the *SHADOW* program (Lai & Cerrina, 1986). The input optical elements are three nickel-coated mirrors and a 5 µm carbon foil. Starting from the source point located 2.9° behind the waist of the bending-magnet centre, we obtained a final image as shown in Fig. 3. With various conditions of optical component errors as specified in Table 2, we confirmed that the distortion and aberration of the imaging system is acceptable to the specification. Wavefront distortion or the image diffuse error by the carbon foil and the scintillation plate were not considered in the ray tracing.

3. Measurements of beam parameters

Transverse beam parameters were measured in the diagnostic beamline. Beam sizes were measured with two 25 µm × 512 pixel linear photodiode arrays and a CCD camera with 9.7 µm × 9.7 µm pixels. A variable attenuator was used in front of the photodiode detector to prevent saturation. To find the diffraction-limited error of the imaging system, the beam size was changed from large to small by varying the coupling. Since the lower limit of the measured beam size converged to 90 µm as the coupling became smaller, the diffraction-limited error was believed to be 90 µm. The true beam size is then calculated from the measured value by subtracting the diffraction-limited error. With a CCD camera and photodiode arrays, the horizontal beam size and vertical beam size were measured as $\sigma_x = 303$ µm and $\sigma_y = 63$ µm. In Fig. 4, the horizontal and vertical beam profiles measured with a CCD camera and photodiode arrays are shown.

Since the CCD exposure time is about 100 ms, the measured beam size would integrate any kind of beam oscillation faster than 10 Hz.

The corresponding beam emittance was 40 nm rad, which is very large compared with the design value of 12.1 nm rad. This is mainly due to the longitudinal beam instability induced by the higher-order modes of the RF cavity. To control the higher-order cavity modes, a precise RF cavity temperature-control system has been completed and is now under temporary operation. When the RF cavity temperature was adjusted carefully to an optimum value, the beam size was reduced to 182 µm. The equivalent emittance is 11.3 nm rad. Further beam studies will be performed to search for the optimum operation condition of the RF cavity.

We used a fast 20 GHz optical-to-electrical (O/E) converter (New Focus 1437) plugged into a 20 GHz sampling oscilloscope (TEK CSA803A) for the measurement of the bunch length. Both components have a 17 ps input and output rise-time. The optical image is guided to the O/E input through a 4 µm single-mode optical fibre. Because of the very small fibre size, the O/E signal is easily lost when there is a change of beam orbit. Two 15 dB 25 GHz amplifiers are used for the amplification of the O/E
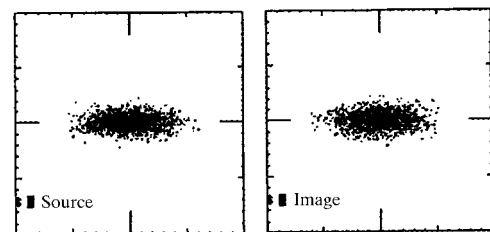
Figure 3
SHADOW ray-tracing result for the X-ray optics. Beam images are plotted in 2 × 2 mm squares.

Figure 2
Band-pass characteristics measured at the detector after three mirrors and a carbon foil.
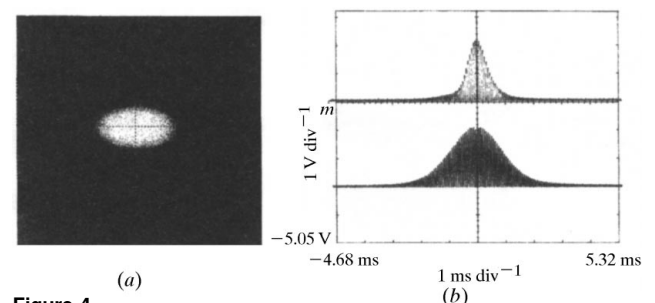
Figure 4
Two beam profiles measured by (*a*) a CCD camera, and (*b*) the photodiode arrays. Beam profiles are automatically Gaussian-fitted using the CCD image, which is not visible here.

output signal. By subtracting the instrumental rise-time effect from the measured value, the true bunch length from the measurement was 33 ps, which is also very long compared with the design value of 17 ps due to the longitudinal beam instability. After the RF cavity temperature control, we obtained 29 ps by the streak-camera measurement.

To measure the bunch structure in the picosecond regime, a 125 MHz synchroscan streak camera (Hamamatsu C5680) with 2 ps resolution was installed on the optical table in the experimental hutch. It is composed of a fast-scan module, a slow-scan module and a synchroscan module. Not only the bunch-structure measurement in the time domain but also spatio-temporal measurement of the bunch train is possible with a slow-scan and a synchroscan module. Fig. 5(a) shows an example of a bunch-train image, oscillating longitudinally, taken by a synchroscan streak camera. The vertical axis is displayed in temporal units (2 ns) and the horizontal axis is displayed in spatio-temporal units (6.4 mm or 500 ns). It represents a longitudinal oscillation, where the phase is modulating between the upper and lower bunches by coupled-bunch instability. Upper and lower bunches are 4 ns delayed in this picture. Fig. 5(b) shows a typical spatio-temporal snapshot of the bunch train. It shows the bunch-train image oscillating transversely due to the transient ion oscillation. The vertical axis is 500 ns temporal scan and the horizontal axis is 6.4 mm or 25 µs spatio-temporal scan. Each bunch train shows the vertical bunch profile in the horizontal direction. One can see the blow-up of bunch size as well as the increase of oscillation amplitude along the bunch train (Huang *et al.*, 1997).
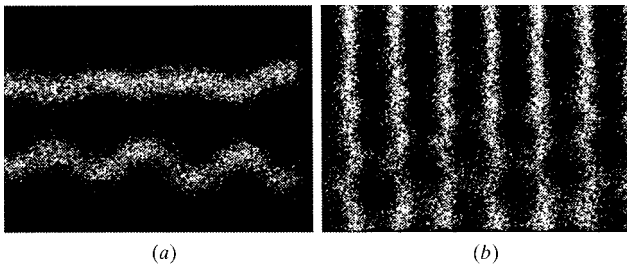
Figure 5
(a) An image taken by dual-axis synchroscan streak camera shows longitudinal phase oscillation. The time delay between the upper and lower bunch is 4 ns. (b) A typical spatio-temporal streak-camera image showing the transient beam-ion oscillation along the bunch train. The vertical axis is 500 ns temporal scan and horizontal axis is 6.4 mm spatial scan (time span = 25 µs). Each bunch train shows a vertical bunch profile only. One can see blow-up of the bunch size as well as the increase of oscillation amplitude along the bunch train.
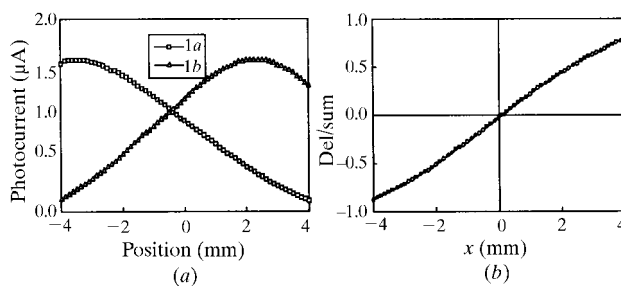
Figure 6
(a) Photocurrent output from the gold electrodes 1a and 1b. (b) Sensitivity (slope of the del/sum curve) of the X-ray position monitor measured in 20 µm steps. Maximum sensitivity is 0.4% µm^{-1} at the centre.

Table 3
Measured and design value of beam profiles.

	Measured value	Design value	Remark
σ_x	303 µm	189 µm	Normal
	182 µm		By RF control
σ_y	63 µm	59 µm	By photodiode array
	<40 µm		By coupling measurement
σ_s	33 ps	17 ps	By photodiode
	29 ps		By streak camera
ε_x	40 nm rad	12.1 nm rad	Normal
	11.3 nm rad		By RF control

Two kinds of beam position monitors are being used in the diagnostic beamline. An X-ray position monitor measures the vertical position, which is made of two gold electrodes diagonally plated on the surface of the beryllium oxide ceramic plate. It was installed in the beamline front-end with a stepper-motor driver. The vertical sensitivity measured with a 2 µm step generator at the centre of the monitor was 0.4% µm^{-1}, as shown in Fig. 6. A quadrant photodiode sensor composed of four photodiode cells measures both the horizontal and vertical beam position with 0.1% µm^{-1} sensitivity using the visible-light beam image. Beam oscillations up to 300 kHz are also observed with a photodiode position sensor.

The various beam parameters measured at the diagnostic beamline are summarized in Table 3. The vertical beam emittance cannot be precisely measured yet because of the diffraction-limited error. We estimated the vertical emittance to be smaller than 11 nm rad from the measurement of the linear coupling (less than 1%) between the horizontal and vertical plane.

4. Conclusions

A visible diagnostic beamline is operating at the PLS for transverse- and longitudinal-beam-profile measurements. Since the diffraction-limited error in the transverse-beam-size measurement is very large, an X-ray imaging system is under construction for the precise measurement of the transverse beam sizes. Major beam instruments in the diagnostic beamline include a CCD camera, linear photodiode arrays, position-sensitive photodiode and an X-ray position monitor. It is also equipped with a 125 MHz synchroscan streak camera and a 17 ps photodiode detector. With this diagnostic beamline, we measured transverse beam profiles, beam position and the longitudinal bunch structure in the picosecond time scale. In particular, with a 2 ps resolution synchroscan streak camera, we studied the spatio-temporal beam properties of the electron beam. Results of the various beam parameter measurements in the visible imaging system are summarized.

References

Huang, J. Y., Kwon, M., Lee, T. Y. & Ko, I. S. (1997). PAL-PUB-97–26. Pohang Accelerator Laboratory, San 31, Hyoja-dong, Pohang 790-784, Korea.
Kirkpatric, P. & Baez, A. V. (1948). *J. Opt. Soc. Am.* **39**, 766–774.
Lai, B. & Cerrina, F. (1986). *Nucl. Instrum. Methods*, A**246**, 337–341.
Rossa, E. (1994). *AIP Conference Proceedings 333*, pp. 148–159. New York: AIP.
Wilke, M. D. (1994). *AIP Conference Proceedings 333*, pp. 128–147. New York: AIP.